New Journal of Physics
The open access journal at the forefront of physics

Deutsche Physikalische Gesellschaft DPG IOP Institute of Physics

PAPER • OPEN ACCESS

Assembly and transport of nematic colloidal swarms above photo-patterned defects and surfaces

To cite this article: Arthur V Straube *et al* 2018 *New J. Phys.* **20** 075006

New Journal of Physics
The open access journal at the forefront of physics

Deutsche Physikalische Gesellschaft DPG
IOP Institute of Physics

Published in partnership with: Deutsche Physikalische Gesellschaft and the Institute of Physics

OPEN ACCESS

RECEIVED
8 February 2018

REVISED
20 April 2018

ACCEPTED FOR PUBLICATION
10 May 2018

PUBLISHED
18 July 2018

PAPER

Assembly and transport of nematic colloidal swarms above photo-patterned defects and surfaces

Arthur V Straube[1,2], **Josep M Pagès**[3,4], **Antonio Ortiz-Ambriz**[2,4], **Pietro Tierno**[2,4,5], **Jordi Ignés-Mullol**[3,4] **and Francesc Sagués**[3,4]

[1] Freie Universität Berlin, Department of Mathematics and Computer Science, Arnimalle 6, D-14195 Berlin, Germany
[2] Departament de Física de la Matèria Condensada, Universitat de Barcelona, E-08028, Barcelona, Catalonia, Spain
[3] Departament de Ciència de Materials i Química Física, Universitat de Barcelona, E-08028, Barcelona, Catalonia, Spain
[4] Institut de Nanociència i Nanotecnologia, IN^{2}UB, Universitat de Barcelona, E-08028, Barcelona, Catalonia, Spain
[5] Universitat de Barcelona Institute of Complex Systems (UBICS), Universitat de Barcelona, E-08028, Barcelona, Catalonia, Spain

E-mail: ptierno@ub.edu

Keywords: liquid crystals, colloids, autonomous actuation, biomimetics

Supplementary material for this article is available online

Abstract

We investigate the dynamic assembly and swarm translocation of anisometric colloidal particles dispersed in a nematic liquid crystal and driven above a photosensitive surface. We use liquid crystal-enabled electrophoresis to propel these particles via an alternating electric field perpendicular to the sample cell. By manipulating the anchoring conditions on one surface of the experimental cell, we obtain a spatially extended spiral pattern of the liquid crystal orientation that induces the dynamic assembly of a rotating colloidal mill. This structure can be transported by translocating the topological defect above the photosensitive surface. We complement our findings with a theoretical model that captures the basic physics of the process, by formulating an analytic equation for the director field above the surface. Our reconfigurable nematic assemblies may be used as a test bed for complex swarming behaviour in biological and artificial microscale systems.

1. Introduction

The formation of coherent structures from a disordered array of interacting, self-propelling elements is currently an active research topic in different fields of science [1–4]. The interest arose from both a fundamental and an applied point of view. On the one hand, monitoring and controlling the transport properties of large populations of artificial micromachines may help understanding the underlying mechanisms that govern spontaneous formation of coherent structures from self-propelled units, as observed in disparate biological systems [5–11]. On the other hand, these investigations have also direct technological applications related with the field of drug delivery in microfluidic and vein networks. In particular, examples include the controlled release of biochemical cargos attached to functionalized colloidal particles [12–15], the miniaturization of simple operations in lab-on-a-chip devices [16–20] or the realization of different functional tasks at the microscale [21–23].

The formation of particle swarms from ensembles of artificial prototypes driven by an external field has been recently reported by different research groups who use electric [24, 25], optic [26] or magnetic fields [27, 28]. In most of the cases, the driven particles are dispersed in an isotropic fluid such as water, and are propelled through lithographic structures or assembled along a circular confinement. An alternative approach that is gaining interest in the community is the use of photosensitive surfaces in a nematic liquid crystal matrix, where the dispersed particles can be driven by an electric field along predefined tracks [29–33]. The use of an anisotropic medium for the particle motion may provide different advantages to self-propelling particle systems. For example the possibility of controlling the mean molecular orientation of the dispersing medium via an external

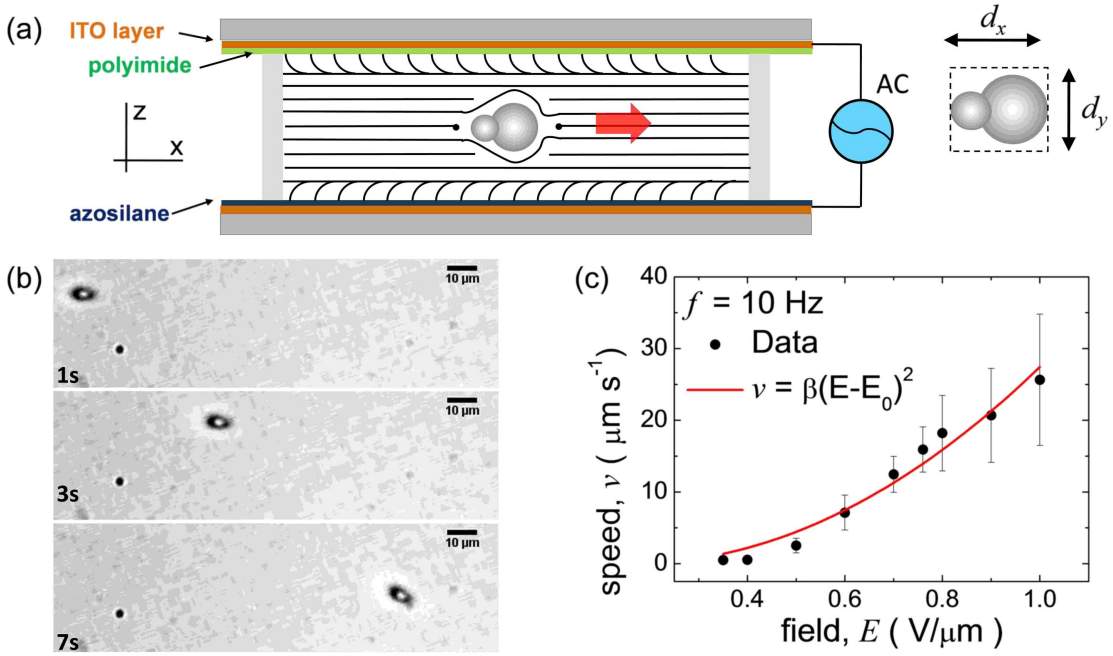

Figure 1. (a) Schematic of the experimental cell showing one anisometric particle enclosed between two ITO plates and dispersed in a nematic liquid crystal of negative dielectric anisotropy. An AC voltage is applied between both plates. The colloid can be characterized by two lateral dimensions (d_x, d_y). (b) Sequence of microscope images showing the controlled propulsion of one particle when subjected to an AC field with amplitude $E = 0.76$ Vμm^{-1} and frequency $f = 10$ Hz. The corresponding video (Video1) can be found in the supporting information which is available online at stacks.iop.org/NJP/20/075006/mmedia. (c) Speed, v, versus amplitude, E, of the applied electric field for an individual anisometric particle. Scattered points are experimental data, continuous red line is a quadratic fit to the data.

field, the ability of switching from an anisotropic to an isotropic medium by varying the system temperature, or finally the absence of hard walls or confinements that may alter the particle motion due to steric constraints.

Motivated by these prospects, in this article we investigate the dynamics of an ensemble of anisometric colloidal particles that are dynamically assembled into a rotating mill organized around a single topological defect of a liquid crystal on a surface that imposes planar alignment. In addition, we study the translocation of the colloidal swarm when the topological defect is relocated on the surface. In this case we observe that the condensed pattern disassembles, forming a polarized phase that moves along the director field. To understand the system dynamics, we theoretically determine the director field in contact with the photosensitive surface, and show that a simple simulation scheme describes well the observed phenomena. Our colloidal model system may be used to explore the rich many-body physics of collective organization and swarming in microscale driven systems, and may also inspire the use of similar strategies to control and guide biological entities along pre-designed paths [33, 34].

The paper is outlined as follows. After the description of the experimental system, in section 2, we discuss the propulsion of a single colloidal particle, section 3. In section 4 we describe the formation of the experimentally observed mill pattern and quantify its properties, which is then followed in section 5 by a comparison with a simple numerical model. An analytic expression for spiral pattern is derived in the appendix. The process of translocation is discussed in section 6, in which we compare the results of the measurements with the predictions of the numerical model. We summarize the results and draw the conclusions in section 7.

2. Experimental system

We prepare thin cells enclosing a solution of colloidal particles dispersed in a nematic liquid crystal (MLC-7029, Merck) characterized by a negative dielectric anisotropy $\Delta\epsilon = -3.6$ (at 1 kHz). As shown in figure 1(a), these cells are composed by two microscope slides with an area of 15 $\times$ 25 mm^2, 0.7 mm thickness, and coated with a thin layer of indium-tin oxide (ITO) with a sheet resistance of ~100 Ω sq (VisionTek Systems). The plates are cleaned by sonication in a 1% Micro-90 (Sigma-Aldrich) solution, rinsed with ultrapure water (18.2 MΩ cm, Millipore Milli-Q), and dried at 80 °C for 30 min. Afterwards, the plates are introduced in a plasma surface treatment equipment (ZEPTO, Diener Electronic). One of the plates is functionalized with a photosensitive surface in a toluene medium (peptide synthesis grade, Scharlau) by mixing two silanes in a ratio 5:1, (3-aminopropyl)triethoxysilane (APTES, Sigma-Adrich) and an azosilane compound, (3)-4-(4-((4-octylphenyl)

diazenyl)phenoxy)-N-(3-(triethoxysilyl)propyl)butanamide (GalChimia). Butylamine is added as catalyzer. The other plate is coated with a thin layer of a polyimide compound (0626 from Nissan Chemical Industries), after plasma surface activation, in order to achieve a strong homeotropic anchoring of the liquid crystal at the surface. Both plates are disposed with the ITO facing inwards and are glued together with a separation of about 23 μm using Mylar spacers (Goodfellow). The anisometric particles used in this work have a pear-like shape with two connected spherical lobes (Magsphere Inc). The particles are made of polystyrene and have lateral dimensions $d_x = 4$ μm, $d_y = 3$ μm, see figure 1(a).

The experimental system is composed of an upright optical microscope (Nikon Eclipse 50iPol) containing two collimated epi-illumination LED light sources of wavelength 455 nm (Thorlabs M455L3, 900 mW) and 365 nm (Thorlabs M365L2, 190 mW). Brightfield illumination for microscopy was performed with a red longpass filter (Lambda 645 nm) to avoid perturbing the azosilane coating [31, 35–37]. The microscope objective is also used to focus light coming from the LEDs onto the sample cell projecting a Gaussian intensity profile. Images of the particle dynamics are recorded with a CMOS camera (AVT Marlin F-131B). The external, alternating current (AC) is applied with a voltage amplifier (TREK model PZD700) controlled by a function generator (Agilent DSOX2002A).

3. Single particle transport

We start by describing the transport properties of an individual anisometric particle. Figure 1(b) illustrates different experimental snapshots of a single particle driven in the liquid crystal (LC). To understand the mechanism of motion, one has to consider the experimental geometry, as schematically depicted in figure 1(a). In the absence of an external field, the homeotropic alignment at the surface of the two cells forces the nematic director $\boldsymbol{n}$ to point along the $\boldsymbol{z}$-axis. Since the LC has a negative dielectric anisotropy, under the applied field $\boldsymbol{n}$ orients perpendicular to the field direction, say along the $\boldsymbol{x}$-axis. As a consequence, also the main axis of the dispersed particle aligns along $\boldsymbol{n}$. Inside the LC, the colloidal particle distorts the nematic matrix creating topological defects around its surface [38]. For our pear-shaped colloids we find two point defects located at both apexes of the particle, in the form of a non-symmetric 'double-boojum' [39].

The applied AC electric field induces electroosmotic flows around the particles. The anisometric shape of particles breaks the symmetry of these flows leading to net phoretic propulsion at speed v [29]. Given the confined geometry, the motion is quasi-two-dimensional, and thermal fluctuations of the particle are negligible due to its relative large size and the high viscosity of the LC medium. Most particles move with their large lobe ahead, and exhibit a ballistic-like trajectory as shown by the sequence of images in figure 1(b) (see also Video1 in the supporting information). Further, we note that, since the AC field is applied perpendicularly to the plane of motion, linear (DC) electrophoretic effects resulting from the attraction toward the two electrodes are also negligible.

The particle phoretic speed v can be controlled by varying the amplitude E of the applied AC field, as shown in figure 1(c). Similarly to [29], we detect a quadratic dependence of v on E typical of electroosmotic flows developing around the particle, $v = \beta(E - E_0)^2$. Note that the propulsion velocity is independent of the polarity of the field, which enables the application of AC fields. From the fit to the experimental data, we determine the threshold field for motion, $E_0 = 0.16 \pm 0.06$ Vμm^{-1}, figure 1(c). Here E_0 represents the minimum field required to generate enough ionic flow around the particle to provide propulsion.

In the collective particle dynamics we will keep the field parameters fixed to $E = 0.76$ Vμm^{-1} and $f = 10$ Hz, which results in an averaged single particle speed of $v = 15.1$ μms^{-1}. Finally, we note that at a fixed amplitude, the frequency dependence $v = v(f)$ is even more complex, due to the nature of the ionic motion within the LC, as reported in previous works [29, 40]. We, therefore, keep the frequency constant through all experiments.

4. Dynamic assembly on a spiral pattern

Controlling the orientation of the director, $\boldsymbol{n}$, allows steering the trajectory of the colloidal particles that are propelled in the LC by the applied AC field. We investigate the collective dynamics of the anisometric particles above a spiral pattern characterized by a central topological defect, which is shown in figure 2(a) under crossed polarizer and analyzer. This complex pattern was obtained with the following steps. First we use UV light to irradiate a large, circular region of the surface coated with the azosilane (see section 2), which forces the dye molecules there to be in the *cis* configuration, i.e. to orient parallel to the surface. Thus, the LC director $\boldsymbol{n}$ acquires a planar anchoring on this area. After that, we irradiate a smaller central spot with blue light, forcing the azosilane layer to revert to the *trans*-configuration. In this situation, the director $\boldsymbol{n}$ acquires a homeotropic alignment inside and outside a circular corona of planar molecules. When the AC field is applied, the LC

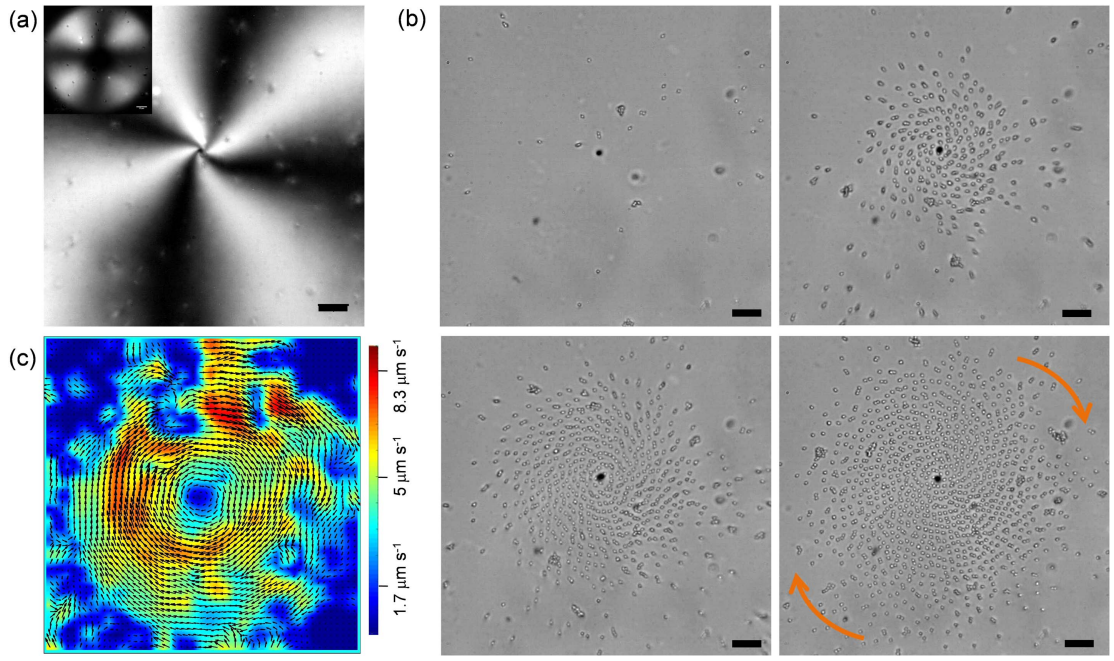

Figure 2. (a) Polarized microscope image taken under crossed polarizer and analyzer, showing the spiral pattern induced by light on the nematic LC due to the irradiated azosilane layer. The small inset at the top shows a photoaligned corona before the application of the AC field. (b) Sequence of experimental images of a mill pattern composed by anisometric colloidal particles assembled around a topological defect (black spots). The applied field has a frequency $f = 10$ Hz and an amplitude $E = 0.76\ \mathrm{V}\mu\mathrm{m}^{-1}$. Scale bars for all images are 25 μm, and all are separated by 37 s. The corresponding video (Video2) can be found in the supporting information, which is available online. (c) Particle image velocimetry of the largest nematic colloidal mill shown in panel (b). The color bar on the right side shows the amplitude of the velocity field.

molecules with planar alignment in this corona extend inwards and outwards, and $\boldsymbol{n}$ forms a spiral pattern with a central topological defect of charge +1, figure 2(a). Indeed, the LC used here is characterized by a bend elastic constant smaller than the splay one, and thus bend distortions are favored during orientation of the LC matrix.

In figure 2(b) we show the dynamic assembly of an ensemble of anisometric particles following this spiral pattern. As shown by the corresponding Video2 in the supporting information, once the external field is applied, particles move towards the topological defect, which appears as a small black spot at the center of the image. Particles follow a spiral trajectory, and once close to the defect they start orbiting around it at a constant distance. As more particles arrive from outside, the density of the rotating cluster increases, until reaching a size of $N \approx 1000$ particles after $t = 113$ s, figure 2(b). The cluster rotates as a solid body around the topological defect, and is completely dynamic in nature, since its structure can be easily disassembled by switching off the field or reducing its strength below E_0 (see section 3). The cluster's rotational motion follows the chirality of the underlying pattern, which is randomly selected upon irradiation, while the particles located in the central denser region keep a constant inter-particle distance larger than the particle diameter. This indicates the presence of a long range repulsive interaction that may arise from the electrostatic dipoles induced by the applied AC field. Another interesting feature is the formation of chains at the periphery of the core. This chaining arises from the LC-mediated quadrupolar elastic interaction induced by the double-boojum defects located at both apexes of the particles. The chains tend to spiral at a certain angle to minimize the elastic energy and ensure the relocation of the incoming particles [38].

In order to analyze the dynamic state, we show in figure 2(c) particle image velocimetry analysis of the colloidal pattern. Indeed, we find that, after a short transient, the cluster of particle organizes into a rotating mill pattern, with an almost constant linear velocity everywhere in the cluster and, thus, with an angular velocity that decays with the distance to the center of the cluster.

5. Theoretical description of the colloidal mill

To model the dynamics of particles assembled in the colloidal mill, we apply the minimal scheme able to capture all the general trends of the dynamic assembly. We consider particles to be spherical with a prescribed phoretic speed and restrict our consideration to the two-dimensional (x, y) plane, which is parallel to the electrodes. The overdamped motion of an ensemble of N colloidal particles with positions $\boldsymbol{r}_i$ $(i = 1, ..., N)$ in a LC matrix is described by the following equations of motion

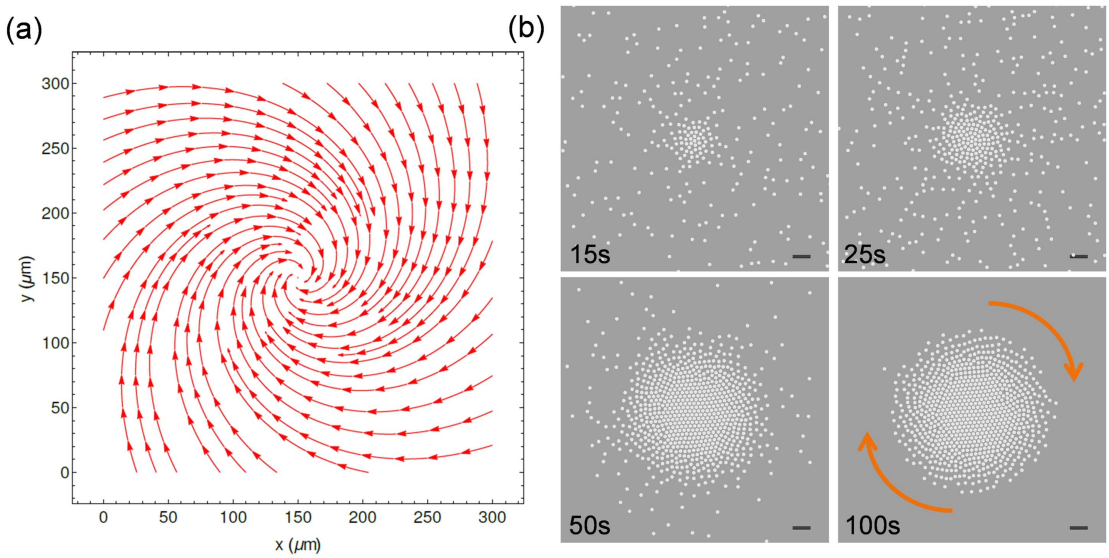

Figure 3. (a) Vector field of the spiral pattern calculated following the model in the text over an area of 300 × 300 μm^2. (b) Results of numerical simulations showing the assembly of $N = 800$ particles above the spiral pattern. Scale bar is 20 μm, see also corresponding Video3 in the supporting information.

$$\frac{\mathrm{d}\boldsymbol{r}_i}{\mathrm{d}t} = v_i(f, E)\boldsymbol{n}(\boldsymbol{r}_i, t) + \zeta_{||}^{-1}\sum_{j\neq i}\boldsymbol{F}_{ij}, \tag{1}$$

where the first term on the right hand side of equation (1) describes the phoretic propulsion of individual particles whose direction is along the local LC director, the second one is a force that accounts for interactions with other particles, and $\zeta_{||}$ denotes the friction coefficient of the particle moving along the director field. This model implies that particles propel strictly along the director field $\boldsymbol{n}(\boldsymbol{r}, t)$ ($|\boldsymbol{n}| = 1$), and the strength of propulsion generally depends on the field parameters (E, f). Since we are only interested in describing the particle dynamics at fixed f and E, we set the strength of propulsion as

$$v_i = v_0(1 + 0.2\xi), \tag{2}$$

where v_0 is the constant deterministic mean speed of the particles and ξ is a Gaussian random variable with zero mean and unit variance. The noise distribution has been measured in experiments, and it is about 20% of the mean particle speed, which is reflected on the weight of this term. This distribution resulted from the presence, in the experimental system, of disorder, surface inhomogeneities and other sources of noise. For the values used in the experiments, $f = 10$ Hz and $E = 0.76$ Vμm^{-1}, we have set $v_0 \approx 15.1$ μms^{-1}.

The director field is modeled as a spiral pattern

$$\boldsymbol{n}(\boldsymbol{r}, t) = \boldsymbol{n}(\psi(\boldsymbol{r} - \boldsymbol{q})), \tag{3}$$

defined by the function ψ, which is obtained in the appendix by minimizing the energy functional of the nematic liquid crystal, and which is given in equation (A.7). In polar coordinates, the director field spirals out of the origin according to $\boldsymbol{n} = (n_\rho, n_\theta) = (\cos\psi, \sin\psi)$. Since we are interested in patterns that spiral in, we flip the sign of the radial component of the director, $n_\rho \to -n_\rho$ and then pass to Cartesian coordinates (x, y). As a result, the components of the director field, $\boldsymbol{n}(\boldsymbol{r}) = (n_x, n_y)$, can be presented as $n_x(\boldsymbol{r}) = -\cos\theta n_\rho - \sin\theta n_\theta = -\cos(\theta(\boldsymbol{r}) - \psi(\boldsymbol{r}))$, $n_y(\boldsymbol{r}) = -\sin\theta n_\rho + \cos\theta n_\theta = -\sin(\theta(\boldsymbol{r}) - \psi(\boldsymbol{r}))$.

The corresponding pattern generated by equation (3) in the domain $0 \leqslant x \leqslant L_x, 0 \leqslant y \leqslant L_y$ with $L_x = 300$ μm and $L_y = 300$ μm and placed at the position $\boldsymbol{q} = (150$ μm, 150 μm) is shown in figure 3(a). The spiral pattern is characterized by the parameters $\alpha_1 = -\pi/5$, $\alpha_2 = -\pi/4$ (see the appendix), and the inner and outer radii are set to $r_1 = 2$ μm and $r_2 = 1000$ μm, respectively. We note that although the pattern is derived for the elastic constants $K_S = 16.1$ pN and $K_B = 15.0$ pN, which are close in value, equation (A.7), valid for $K_S \neq K_B$, gives a slightly different pattern with respect to the one-constant approximation, equation (A.8), but it represents a more accurate solution.

In figure 3(b) we show the result from a numerical simulation, where $N = 800$ particles are assembled above the spiral pattern (see also the corresponding Video3 in the supporting information). In order to reproduce the dynamic features observed in the experimental system, we introduce long-range repulsive interaction between the colloidal particles. We have checked and found that different long-range repulsion potentials seem to work fine to describe the dynamics of the colloidal assembly process. To be specific, in the control simulations we stick to the repulsive potential of the form $U_1(r_{ij}) \propto 1/r_{ij}^3$, which leads to the repulsive force exerted on particle i by

particle j

$$\boldsymbol{F}_{ij}^{(1)} = -\frac{\partial U_1(r_{ij})}{\partial \boldsymbol{r}_i} = \frac{C_1 \boldsymbol{r}_{ij}}{r_{ij}^5}, \tag{4}$$

where $\boldsymbol{r}_{ij} = \boldsymbol{r}_i - \boldsymbol{r}_j$, $r_{ij} = |\boldsymbol{r}_{ij}|$. The constant $C_1/\zeta_{||}$ is taken as 2000 μm^{5}s^{-1} in the simulations. We note that this law of repulsion is a justified assumption because the particles are polarized in the applied AC field and acquire an electric dipole moment [41, 42]. This dipole is always perpendicular to the electrodes and to the plane of particles, and therefore all the dipole moments stay parallel to each other. As a result, they are expected to repel according to the above dipolar interaction force.

To account for a finite size of particles, we also introduce a steep short-range repulsive potential of the form $U_2(r_{ij}) \propto (\sigma/r_{ij})^{48} - (\sigma/r_{ij})^{24} + 1/4$, which is applied at distances $r_{ij} < r_0 = 2^{1/24}\sigma$ and is vanishing otherwise. Here, σ is an effective diameter of the particle. At short distances, $r_{ij} < r_0$, this potential leads to the strictly repulsive force

$$\boldsymbol{F}_{ij}^{(2)} = -\frac{\partial U_2(r_{ij})}{\partial \boldsymbol{r}_i} = 24C_2\left[2\left(\frac{\sigma}{r_{ij}}\right)^{48} - \left(\frac{\sigma}{r_{ij}}\right)^{24}\right]\frac{\boldsymbol{r}_{ij}}{r_{ij}^2}. \tag{5}$$

In our study, we set $C_2/\zeta_{||} \approx 1\ \mu\text{m}^2 \cdot \text{s}^{-1}$ and $\sigma = 5\ \mu$m. Note that σ is slightly larger than the actual size of particles, d_x, d_y. To better replicate the experimental observations, we assume that defects in the liquid crystal in the vicinity of particles prevent the direct contact of particles, leading to a larger effective hard core distance.

Finally, we also account for quadrupolar interactions, which cause a weak chaining of particles depending on the underlying pattern. The corresponding force can be represented as [43]

$$\boldsymbol{F}_{ij}^{(3)} = -\frac{\partial U_3(r_{ij})}{\partial \boldsymbol{r}_i}, \quad U_3(r_{ij}) = \frac{C_3}{r_{ij}^5}(3 - 30\cos^2\vartheta + 35\cos^4\vartheta), \tag{6}$$

where ϑ is the angle between the far-field orientation of the nematic director $\boldsymbol{n}$ and the vector connecting the center of particles, $\boldsymbol{r}_{ij}$. In the simulations, we set $C_3/\zeta_{||} = 500\ \mu\text{m}^7 \cdot \text{s}^{-1}$. Note that figure 3(b) reflects the consequence of these interactions leading to spiral chaining at the periphery of the hard core.

The comparison between the experimental and numerical data is shown in figure 4, where we plot different observables related with the dynamics of the colloidal mill as obtained in experiments (figures 4(a), (b)) and simulations (figures 4(c) and (d)). In the former case, we use video microscopy and tracking routines [44] to extract the positions (x_i, y_i) of each particle i, and analyze the radial and azimuthal particle velocities averaged over the ensemble, (v_ρ, v_θ) with $v_{\rho,\theta} = \sum_i v_{\rho,\theta}^{(i)} / \sum_i |\boldsymbol{v}_i|$, as measured in polar coordinates from the central defect. Both quantities are shown in figure 4(a) for the rotating mill, and compared with the numerical case in figure 4(c). Both types of data present the same trend, with a vanishing radial velocity when the mill is formed and an azimuthal component that approaches -1. Both quantities are negative since the particles are moving toward the center thus against the radial direction, outwards by definition ($v_\rho < 0$), and in a clockwise sense ($v_\theta < 0$). The main difference between experiments and simulations refer to transient states determined by initial conditions, which are clearly different in both cases. As expected, the convergence to the final state shows similar trends in the evolution of v_ρ and v_θ.

Apart from the instantaneous velocity, we characterize the dynamics in terms of two other order parameters that describe, respectively, the degree of particle alignment and collective rotation. The first one is the normalized polarity P of the pattern, defined as:

$$P = \left| \frac{\sum_i \boldsymbol{v}_i}{\sum_i |\boldsymbol{v}_i|} \right|, \tag{7}$$

with $\boldsymbol{v}_i$ being the velocity of particle i at position $\boldsymbol{r}_i$ from the center of mass of the ensemble, and the summation is performed over all particles in the ensemble. The second parameter is the normalized angular momentum of the particle ensemble, defined as

$$M = \left| \frac{\sum_i \boldsymbol{r}_i \times \boldsymbol{v}_i}{\sum_i |\boldsymbol{r}_i||\boldsymbol{v}_i|} \right|. \tag{8}$$

As described in [45], both order parameters are necessary to quantitatively determine whether the collection of propelling particles is in a coherent flock state (high value of P, low M) or in a single-mill state (low P, high M). As shown in figures 4(b) and (d), we find that in the experiments and simulations both assemblies show a negligible polarity P, while the angular momentum M increases toward unity.

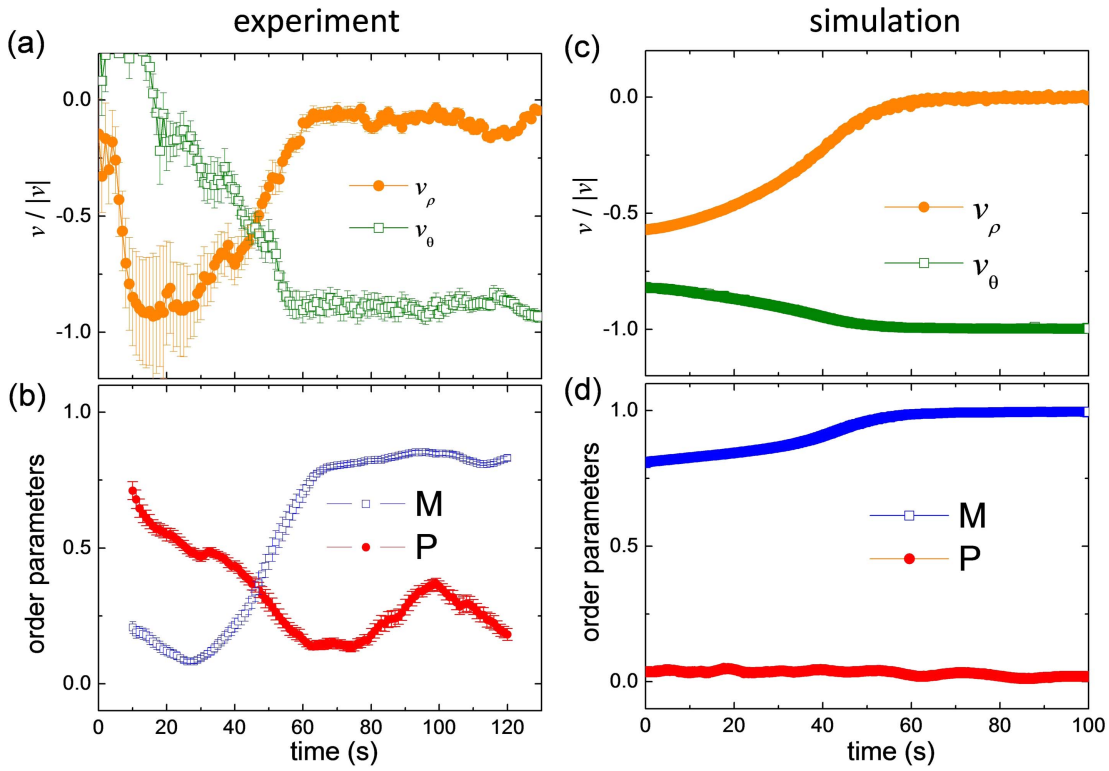

Figure 4. (a)-(d) Comparison between results from experiments (a), (b) and numerical simulations (c), (d). The two top graphs (a), (c) show the time evolution of the instantaneous azimuthal (v_θ) and radial (v_ρ) velocities averaged over the number of particles. The two bottom panels (b), (d) show the normalized order parameters polarity P and angular momentum M versus time.

6. Colloidal translocation: experimental and numerical results

While we just described the formation of a colloidal mill, the photosensitive surface also allows to transport these dynamic states everywhere within the cell. For a given assembly, particle speed due to liquid crystal-enabled electrophoresis (LCEEP) drops down to zero at electric field frequencies of about 50 Hz. For greater stability, we choose 1 kHz as the frequency to freeze the assembly in place, while we pull the topological defect from the initial position (center of the formed colloidal mill) for a certain distance. This translocation is performed through a disclination line that forms as the UV light spot is dragged between the initial and the final destination on the photosensitive surface. We demonstrate this feature in the sequence of images in figure 5(a), where a mill pattern is translocated a distance of 175 μm (see also Video4 in the supporting information). During translocation, the colloidal swarm moves as a polarized pattern developing a leading edge that is followed by all other particles. These dynamic features are reflected in figure 5(b), where we evaluate the corresponding two order parameters M and P. A colloidal mill is initially assembled under $f = 10$ Hz. It is subsequently held in place by switching to $f = 1$ kHz and a UV light spot is dragged from the center of the mill to a destination spot (figure 5(a)). When the frequency is switched back to 10 Hz, LCEEP becomes active again, dismantling the assembly as particles are driven towards the destination spot. Both order parameters rapidly exchange values raising the value of P and reducing the rotational motion (thus M). The particles move at a constant speed towards the translocated topological defect, raising the value of P to unity, while M vanishes. After 150 s, enough particles have gathered around the destination spot for the mill pattern to form again, thus increasing the corresponding value of M and reducing the degree of alignment of the propelled particles, thus lowering P.

In order to reproduce numerically the experimental situation illustrated in figure 5, we perform a procedure similar to the experimental one. In particular, the operation of transferring one defect from one initial position to a new one at a certain distance is obtained by switching from one spiral pattern to another one with a shifted position after a time t_1

$$\boldsymbol{n}(\boldsymbol{r},\, t) = \begin{cases} \boldsymbol{n}(\psi_1(\boldsymbol{r} - \boldsymbol{q}_1)), & 0 \leqslant t < t_1, \\ \boldsymbol{n}(\psi_2(\boldsymbol{r} - \boldsymbol{q}_2)), & t \geqslant t_1, \end{cases} \tag{9}$$

where the two patterns are determined by the functions ψ_1 and ψ_2 and $\boldsymbol{q}_1$ and $\boldsymbol{q}_2$ specify their locations. The two patterns in equation (9) are generated using equation (A.7) as shown in figure 6(a).

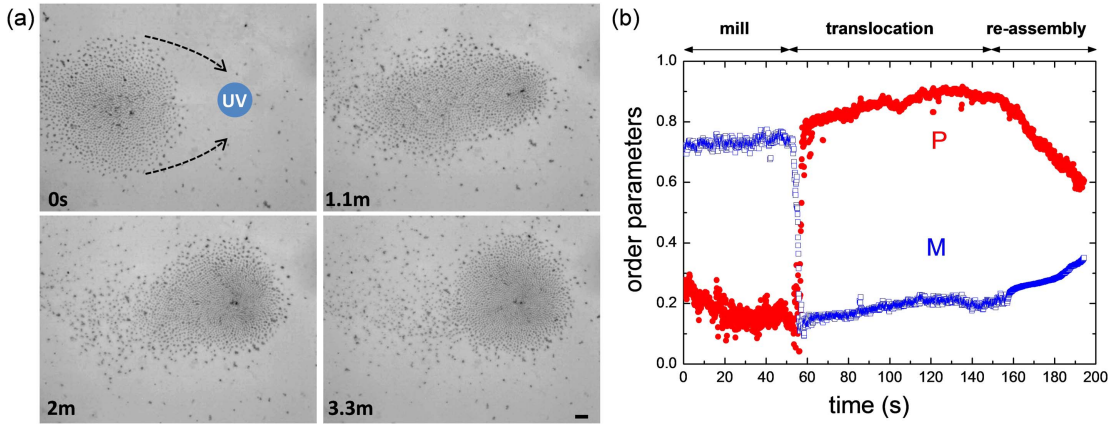

Figure 5. (a) Images showing a colloidal mill that is translocated to a different place of the experimental cell due to *in situ* reconfiguration of the LC field with UV light (365 nm). The blue disk in the first image indicates the location of the translocated topological defect. The experiments were performed with an AC field of amplitude $E = 0.76\ \mathrm{V}\mu\mathrm{m}^{-1}$ and frequency $f = 10$ Hz. The corresponding video (Video4) can be found in the supporting information. Scale bar is 20 μm. (b) Orders parameters P and M measured from the particle trajectories.

We then simulate the translocation process using equation (1) for $N = 1000$ particles in a simulation domain corresponding to a rectangular box, $0 \leqslant x \leqslant L_x, 0 \leqslant y \leqslant L_y$ with $L_x = 500\ \mu$m and $L_y = 675\ \mu$m. Spiral patterns 1 and 2 in equation (9) are characterized by the functions ψ_1 with $\alpha_1 = \pi/6, \alpha_2 = \pi/4$ located at $\boldsymbol{q}_1 = (250\ \mu\mathrm{m},\ 250\ \mu\mathrm{m})$ and ψ_2 with $\alpha_1 = \pi/6, \alpha_2 = -\pi/10$ located at $\boldsymbol{q}_2 = (415\ \mu\mathrm{m},\ 250\ \mu\mathrm{m})$, respectively. Other parameters are kept the same, as for the case of mill.

Figure 6(b) shows the results of the numerical simulations (see also Video5 in the supporting information) with the corresponding calculated order parameters M and P shown in figure 6(c). At time $t = 0$, the particles are uniformly distributed within a circle of radius 200 μm centered at (200 μm, 200 μm). They start to move along the spiral orbits towards the center of attraction, $\boldsymbol{q}_1$, forming a rotating mill. During this process, both parameters, P and M, are non-vanishing and their evolution have opposite tendencies following the previously identified trends.

The switch from pattern 1 to pattern 2 occurs at $t = t_1 = 50$ s, when the behavior of P and M displays an abrupt jump caused by the instant shift of the 'center of attraction' and particle propulsion towards position 2. In contrast to this instantaneous switch, reconstruction of the destination mill is gradual, in analogy with the experiments, as can be seen from the smooth decrease in P and increase in M. Eventually, the center of mass of particles nearly reaches the position of the spiral pattern, $\boldsymbol{q}_2$ and we observe another rotating mill. This state approximately corresponds to $P \approx 0$ and $M \approx 1$.

7. Conclusions

In this article we have demonstrated a method to trap and transport a large ensemble of anisometric colloids dispersed in a nematic liquid crystal matrix and driven by nonlinear electrophoresis. The particles are propelled above a photosensitive surface where a topological defect generating a spiral pattern is created or erased by light. The experiments are combined with a theoretical model that calculates the pattern topology and explains the observed dynamic states and how they depend on the underlying pattern orientation. While our colloidal swarm was transported along a simple track, namely a line connecting two topological defects, in principle more complex patterns may be easily designed to steer the colloidal motion. The advantages of this method over other strategies to propel microscale matter in viscous fluids are the possibility to control the mean molecular orientation of the dispersing medium using an external field, and the independent control of the surface topology through optical means. These two external fields are uncoupled and can be easily interchanged during the experiments, a feature that gives further functionality to the transport in colloidal systems.

Acknowledgments

We thank Lutz Schimansky-Geier, Igor M Sokolov, and Oksana V Manyuhina for stimulating discussions. AVS acknowledges partial support by Deutsche Forschungsgemeinschaft (DFG) through grant SFB 1114, Project C01. JMP acknowledges funding from the European Union's Horizon 2020 Fetopen 'AbioMatter', grant No. 665440. Experiments were funded by MINECO Project FIS2016-78507-C2-1-P. AOA acknowledges support

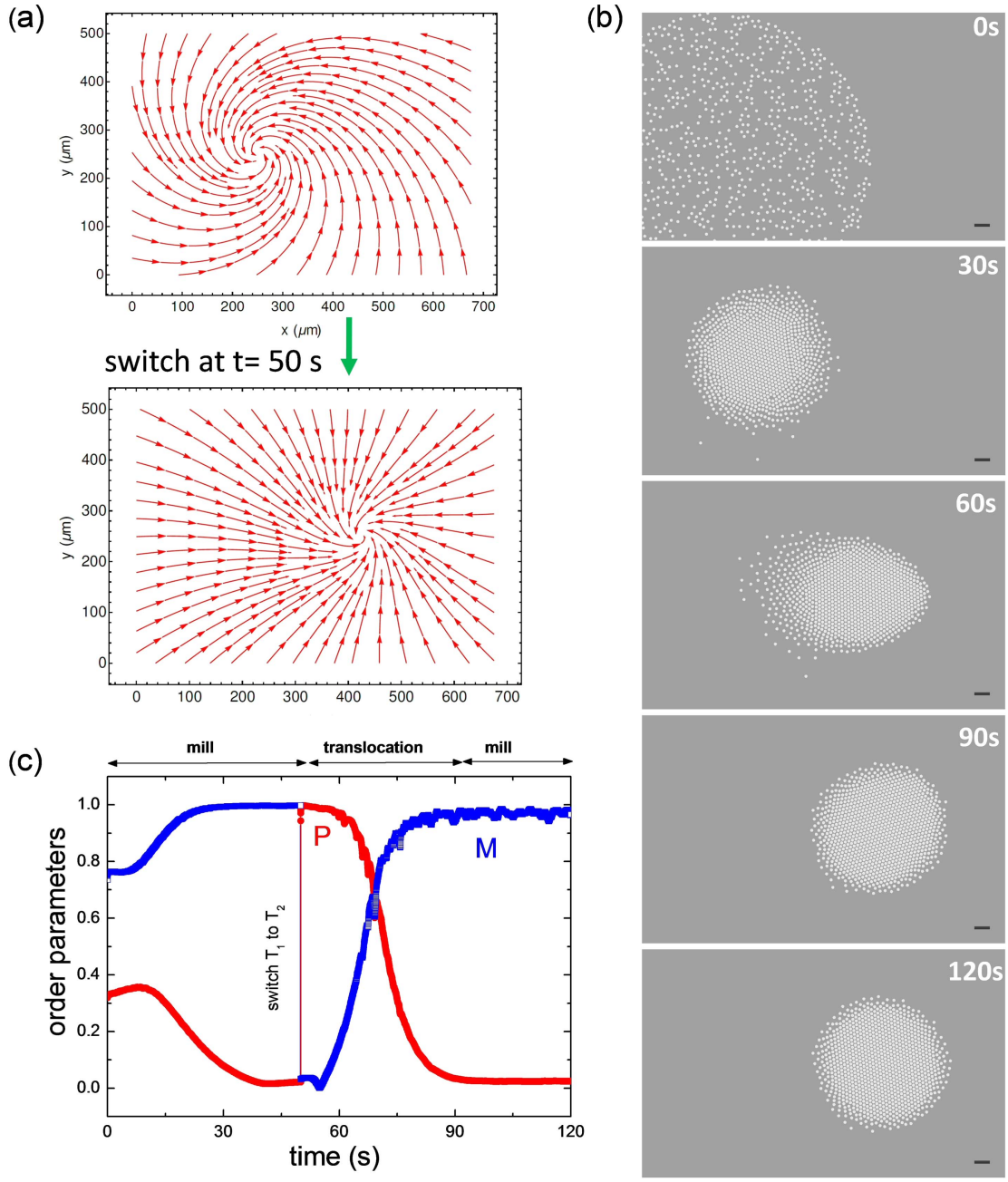

Figure 6. (a) Top (Bottom) image shows the vector field of the spiral pattern obtained for $\alpha_1 = \pi/6, \alpha_2 = \pi/4$ ($\alpha_1 = \pi/6$, $\alpha_2 = -\pi/10$). Both vector fields cover the same area ($500 \times 675\ \mu m^2$) and are exchanged in the simulation after $t_1 = 50$ s. (b) Sequence of images from numerical simulation showing the translocation process for $N = 1000$ particles. First ($t < t_1$) a colloidal mill is assembled above the pattern shown in the top figure 6(a), and later ($t > t_1$) is translated by switching the underlying pattern, bottom figure 6(a). Scale bars for all the images are 20 μm. See corresponding Video5 in the supporting information. (c) Corresponding normalized order parameters M and P versus time.

from the Juan de la Cierva program (FJCI-2015-25787). AOA and PT acknowledge support from the European Research Council (grant agreement No. 335040), MINECO (FIS2016-78507-C2-2-P) and DURSI (2014-SGR-878).

Appendix. Plane spiral patterns of the director field in a nematic liquid crystal

To model mill patterns, here we are interested in finding spiral solutions of the director field that are consistent with the continuum theory of liquid crystals and at the same time can be adjusted to render the experimental conditions. A simple 'magic spiral' solution for a nematic liquid crystal confined by two concentric cylinders of radii $r_1 < r_2$ was obtained by Parodi, see [46]:

$$\psi(\rho) = \frac{\pi}{2}\frac{\ln(\rho/r_1)}{\ln(r_2/r_1)}, \tag{A.1}$$

showing a monotonic change of the angle made by the director with the radial direction. It is based on three basic assumptions: (i) the director field is restricted to the plane normal to the axes of the cylinders; (ii) the anchoring is homeotropic (normal director) at the inner cylinder and planar (tangential director) at the outer one; (iii) the one-constant approximation, implying that the splay, K_S, and bend, K_B, constants are equal.

Later, Williams went beyond the one-constant approximation and also extended the analysis to an arbitrary alignment at the outer boundary but kept it homeotropic at the inner one [47]. However, to achieve a reasonable agreement with the experiment, it is crucial for us to be able to arbitrarily adjust the alignement of the director field also at the inner border. Furthermore, the radial dependence of the angle $\psi(r)$ can be non-monotonic even at slightly different constants, which may become important for describing spiral patterns at large distances. Therefore, for the sake of generality, we will stick to the case $K_S \neq K_B$ and adapt the discussed solutions.

We start by formulating the Frank–Oseen free energy of the nematic liquid crystal. For the two-dimensional case as in assumption (i) above ($n_z = 0$), the corresponding energy expressed as a function of the director field $\boldsymbol{n} = \boldsymbol{n}(\boldsymbol{r})$ and written per unit length along the cylinder is

$$F = \frac{1}{2}\int \mathrm{d}\boldsymbol{r}\,\{K_S(\nabla\cdot\boldsymbol{n})^2 + K_B[\boldsymbol{n}\times(\nabla\times\boldsymbol{n})]^2\}. \tag{A.2}$$

We now proceed to the polar coordinates (ρ, θ) and represent the director field as $(n_\rho, n_\theta) = (\cos\psi, \sin\psi)$ with $\psi = \psi(\rho)$. Using this ansatz in equation (A.2), integrating it over the polar angle θ and introducing the combinations of elastic constants, $K_\pm = (K_S \pm K_B)/2$, we obtain

$$F = \pi\int_{r_1}^{r_2} \rho\mathrm{d}\rho\left[K_+\left(\psi_\rho^2 + \frac{1}{\rho^2}\right) - K_-\left(\psi_\rho^2\cos 2\psi - \frac{2\psi_\rho \sin 2\psi}{\rho} - \frac{\cos 2\psi}{\rho^2}\right)\right].$$

This expression is simplified in terms of a rescaled radial coordinate, $s(\rho) = \ln(\rho/r_1)$, resulting in

$$F = \pi\int_0^{s_2} \mathrm{d}s\,[K_+(\psi_s^2 + 1) - K_-(\psi_s^2\cos 2\psi - 2\psi_s \sin 2\psi - \cos 2\psi)], \tag{A.3}$$

where $s(r_1) = 0$ and $s_2 = s(r_2) = \ln(r_2/r_1)$. Here, the subscripts '$\rho$' and '$s$' denote the corresponding derivatives.

Applying a standard procedure to minimize the energy functional (A.3), we arrive at an ordinary differential equation for $\psi(s)$

$$(K_+ - K_-\cos 2\psi)\psi_{ss} + K_-\psi_s^2 \sin 2\psi + K_- \sin 2\psi = 0, \tag{A.4}$$

which is supplemented by the boundary conditions

$$\psi(0) = \alpha_1, \quad \psi(s_2) = \alpha_2. \tag{A.5}$$

The values α_1 and α_2 determine the arbitrary alignments of the director field at the inner ($\rho = r_1$) and outer ($\rho = r_2$) borders, respectively.

The boundary value problem described by equations (A.4) and (A.5) admits two simple fundamental solutions. One is given by $\psi(s) = \alpha_1 = \alpha_2 = 0, \pi$. The sink-like pattern with $\psi(s) = \pi$ corresponds to an aster, $\boldsymbol{n} = (n_\rho, n_\theta) = (-1, 0)$, while the source-like pattern $\psi(s) = 0$ describes an antiaster, $\boldsymbol{n} = (n_\rho, n_\theta) = (1, 0)$. Another important solution is given by $\psi(s) = \alpha_1 = \alpha_2 = \pm\pi/2$, which corresponds to a vortex, $\boldsymbol{n} = (n_\rho, n_\theta) = (0, \pm 1)$, where the upper and lower signs are for counter- and clockwise directions of rotation, respectively. Because of nonlinearity of equation (A.4), it admits no exact analytic solution for a spiral pattern and should be obtained numerically.

To make an analytical progress, we resort to the approximation of weak distortion, $\psi \ll 1$. By retaining the leading terms only, we end up with the linear ordinary differential equation

$$\psi_{ss} + k^2\psi = 0, \quad k^2 = \frac{2K_-}{K_+ - K_-} = \frac{K_S - K_B}{K_B}. \tag{A.6}$$

Solving equation (A.6) for the case $K_S > K_B$, as in the experiment, and satisfying boundary conditions, equation (A.5), yields

$$\psi(\rho) = \alpha_1\cos(ks(\rho)) + \frac{\alpha_2 - \alpha_1\cos ks_2}{\sin ks_2}\sin(ks(\rho)) \quad (K_S > K_B). \tag{A.7}$$

Note that the solution in the opposite case of $K_S > K_B$ is given by equation (A.7) with trigonometric functions replaced by their corresponding hyperbolic counterparts. The special case of $\alpha_1 = 0$ is in agreement with the results of Williams [47].

The partial case of one-constant approximation, $K_S = K_B$, follows from equation (A.7) in the limit $k \to 0$,

$$\psi(\rho) = \alpha_1 + (\alpha_2 - \alpha_1)\frac{\ln(\rho/r_1)}{\ln(r_2/r_1)} \quad (K_S = K_B), \tag{A.8}$$

which can alternatively be figured out directly from equation (A.4) for $K_- = 0$. Again, the special case of $\alpha_1 = 0$ and $\alpha_1 = \pi/2$ is in agreement with the results by Parodi [46], see equation (A.1). We finally stress that in contrast to one-constant approximation solution (A.8) with a strictly monotonic dependence of $\psi(\rho)$ for $0 \leqslant \alpha_1$, $\alpha_2 \leqslant \pi/2$, $r_1 \leqslant \rho \leqslant r_2$, the corresponding solution (A.7) is more general, leading to periodic radial undulations of the director field for $K_S > K_B$.

ORCID iDs

Antonio Ortiz-Ambriz https://orcid.org/0000-0002-8302-0861
Pietro Tierno https://orcid.org/0000-0002-0813-8683
Jordi Ignés-Mullol https://orcid.org/0000-0001-7963-3799

References

[1] Ramaswamy S 2010 The mechanics and statistics of active matter *Annu. Rev. Condens. Matter. Phys.* **1** 323–45
[2] Koch D L and Subramanian G 2011 Collective hydrodynamics of swimming microorganisms: living fluids *Annu. Rev. Fluid Mech.* **43** 637–59
[3] Vicsek T and Zafeiris A 2012 Collective motion *Phys. Rep.* **517** 71–140
[4] Marchetti M C, Joanny J F, Ramaswamy S, Liverpool T B, Prost J, Rao M and Simha R A 2013 Hydrodynamics of soft active matter *Rev. Mod. Phys.* **85** 1143–89
[5] Nédélec F J, Surrey T, Maggs A C and Leibler S 1997 Self-organization of microtubules and motors *Nature* **389** 305–8
[6] Kunz H and Hemelrijk C K 2003 Artificial fish schools: collective effects of school size, body size, and body form *Artif. Life* **9** 237–53
[7] Couzin I D, Krause J, Franks N R and Levin S A 2005 Effective leadership and decision making in animal groups on the move *Nature* **433** 513–6
[8] Riedel I H, Kruse K and Howard J 2005 A self-organized vortex array of hydrodynamically entrained sperm cells *Science* **309** 300–3
[9] Karsenti E 2008 Self-organization in cell biology: a brief history *Nat. Rev. Mol. Cell Biol.* **9** 255–62
[10] Schaller V, Weber C, Semmrich C, Frey E and Bausch A R 2010 Polar patterns of driven filaments *Nature* **467** 73–7
[11] Sanchez T, Chen D T N, DeCamp S J, Heymann M and Dogic Z 2005 Spontaneous motion in hierarchically assembled active matter *Nature* **491** 431
[12] Guo S, Pan Q and Khamesee M B 2008 Development of a novel type of microrobot for biomedical application *Microsyst. Technol.* **14** 307
[13] Anirudhan T S and Sandee S 2012 Synthesis, characterization, cellular uptake and cytotoxicity of a multi-functional magnetic nanocomposite for the targeted delivery and controlled release of doxorubicin to cancer cells *J. Mater. Chem.* **22** 12888–99
[14] Kim S, Qiu F, Kim S, Ghanbari A, Moon C, Zhang L, Nelson B J and Choi H 2012 Fabrication and characterization of magnetic microrobots for three-dimensional cell culture and targeted transportation *Adv. Mater.* **25** 5863
[15] Garg T, Rath G and Goyal A K 2015 Colloidal drug delivery systems: current status and future directions *Crit. Rev. Ther. Drug. Carrier Syst.* **32** 89–147
[16] Tierno P, Golestanian R, Pagonabarraga I and Sagués F 2008 Magnetically actuated colloidal microswimmers *J. Phys. Chem.* B **112** 16525–8
[17] Pak O S, Gao W, Wang J and Lauga E 2011 High-speed propulsion of flexible nanowire motors: theory and experiments *Soft Matter* **7** 8169–81
[18] Sanchez S, Solovev A A, Harazim S M and Schmidt O G 2011 Microbots swimming in the flowing streams of microfluidic channels *J. Am. Chem. Soc.* **133** 701
[19] Baraban L, Harazim S M, Sanchez S and Schmidt O G 2015 Chemotactic behavior of catalytic motors in microfluidic channels *Angew. Chem.* **125** 5662–6
[20] Barbot A, Decanini D and Hwang G 2015 On-chip microfluidic multimodal swimmer toward 3D Navigation *Sci. Rep.* **6** 19041
[21] Snezhko A and Aranson I S 2011 Magnetic manipulation of self-assembled colloidal asters *Nat. Mater.* **10** 698–703
[22] Martinez-Pedrero F and Tierno P 2015 Magnetic propulsion of self-assembled colloidal carpets: efficient cargo transport via a conveyor-belt effect *Phys. Rev. Appl.* **3** 051003
[23] Massana-Cid H, Martinez-Pedrero F, Navarro-Argemí E, Pagonabarraga I and Tierno P 2017 Propulsion and hydrodynamic particle transport of magnetically twisted colloidal ribbons *New J. Phys.* **19** 103031
[24] Bricard A, Caussin J-B, Desreumaux N, Dauchot O and Bartolo D 2013 Emergence of macroscopic directed motion in populations of motile colloids *Nature* **95** 503
[25] Yan J, Han M, Zhang J, Xu C, Luijten E and Granick S 2016 Reconfiguring active particles by electrostatic imbalance *Nat. Mater.* **15** 1095–9
[26] Lozano C, ten Hagen B, Lowen H and Bechinger C 2016 Phototaxis of synthetic microswimmers in optical landscapes *Nat. Commun.* **7** 12828
[27] Driscoll M, Delmotte B, Youssef M, Sacanna S, Donev A and Chaikin P 2017 Unstable fronts and motile structures formed by microrollers *Nat. Phys.* **13** 375–9
[28] Kaiser A, Snezhko A and Aranson I S 2017 Flocking ferromagnetic colloids *Sci. Adv.* **3** e1601469
[29] Lavrentovich O D, Lazo I and Pishnyak O P 2010 Nonlinear electrophoresis of dielectric and metal spheres in a nematic liquid crystal *Nature* **467** 947–50
[30] Zhou S, Sokolov A, Lavrentovich O D and Aranson I S 2014 Living liquid crystals *Proc. Natl Acad. Sci. USA* **111** 11265
[31] Hernandez-Navarro S, Tierno P, Ignes-Mullol J and Sagues F 2014 Reconfigurable swarms of nematic colloids controlled by photoactivated surface patterns *Angew. Chem., Int. Ed.* **53** 10696–700

[32] Lavrentovich O D 2015 Active colloids in liquid crystals *Curr. Opin. Coll. Int. Sci.* **21** 97–109
[33] Peng C, Turiv T, Guo Y, Wei Q-H and Lavrentovich O D 2016 Command of active matter by topological defects and patterns *Science* **354** 882–5
[34] Guillamat P, Ignés-Mullol J and Sagués F 2016 Control of active liquid crystals with a magnetic field *Proc. Natl Acad. Sci. USA* **113** 5498–502
[35] Hernandez-Navarro S, Tierno P, Ignes-Mullol J and Sagues F 2015 Nematic colloidal swarms assembled and transported on photosensitive surfaces *IEEE Trans. NanoBiosci.* **14** 267
[36] Hernandez-Navarro S, Tierno P, Ignes-Mullol J and Sagues F 2015 Reconfigurable swarms of colloidal particles electrophoretically driven in nematic liquid crystals *Mol. Cryst. Liq.Cry* **610** 163–72
[37] Oswald P and Ignes-Mullol J 2017 Modeling a photoinduced planar-to-homeotropic anchoring transition triggered by surface azobenzene units in a nematic liquid crystal *Phys. Rev.* E **96** 032704
[38] Stark H 2001 Physics of colloidal dispersions in nematic liquid crystals *Phys. Rep.* **351** 387–474
[39] Poulin P and Weitz D A 1998 Inverted and multiple nematic emulsions *Phys. Rev.* E **57** 626–37
[40] Hernandez-Navarro S, Tierno P, Ignes-Mullol J and Sagues F 2015 Electrophoresis of microdroplets in anisotropic liquids: transport, assembling and reaction *Soft Matter* **9** 7999
[41] Squires T M and Bazant M Z 2004 Induced-charge electro-osmosis *J. Fluid Mech.* **509** 217–52
[42] Murtsovkin V A 1996 Nonlinear flows near polarized particles *Colloid J.* **58** 341–9
[43] Poulin P, Stark H, Lubensky T C and Weitz D A 1997 Novel colloidal interactions in anisotropic fluids *Science* **275** 1770
[44] Crocker J C and Grier D G 1996 Methods of digital video microscopy for colloidal studies *J. Colloid Interface Sci.* **179** 298
[45] Chuang Y-L, D'Orsogn M R, Marthaler D, Bertozzi A L and Chayes L S 1998 State transitions and the continuum limit for a 2D interacting, self-propelled particle system *Physica* D **232** 33–47
[46] de Gennes P G and Prost J 1993 *The Physics of Liquid Crystals* (Oxford: Clarendon)
[47] Williams D R M 1994 Nematic liquid crystals between antagonistic cylinders: spirals with bend-splay director undulations *Phys. Rev.* E **50** 1686–7